Formation of Branched ZnO Nanowires from Solvothermal Method and Dye-Sensitized Solar Cells Applications

Hsin-Ming Cheng,[†] Wei-Hao Chiu,[†] Chia-Hua Lee,[‡] Song-Yeu Tsai,[‡] and Wen-Feng Hsieh*,[†]

Department of Photonics and Institute of Electro-Optical Engineering, National Chiao Tung University, 1001 Tahsueh Road., Hsinchu 30050, Taiwan, Republic of China, and Photovoltaics Technology Center, Industrial Technology Research Institute, Hsinchu 310, Taiwan, Republic of China

Branched ZnO nanowires have been fabricated on conductive glass substrates via a solvothermal method for dye-sensitized solar cells (DSCs). The 1D branched nanostructures can afford a direct conduction pathway instead of interparticle hops while using nanoparticles. Furthermore, the short-circuit current density and the energy conversion efficiency of the branched ZnO nanowire DSCs are 4.27 mA/cm^2 and 1.51%, which are twice as high as the bare ZnO nanowire ones. The improvement was a consequence of the enlargement of the internal surface area within the photoelectrode and allowed us to achieve higher dye adsorption to significantly enhance the performance of the DSCs.

I. Introduction

Dye-sensitized solar cells (DSCs) have exhibited solar energy-conversion efficiency of over 10% and remain one of the most promising candidates, as they possess advantages of being flexible, inexpensive, and easier to manufacture than brittle silicon solar cells.[1,2] A very important feature of DSCs is the photoelectrode, which includes mesoporous wide-bandgap oxide semiconductor films with an enormous internal surface area, typically a thousand times larger than those of bulk films.[3–5] To date, the highest solar-to-electric conversion efficiency has been achieved with films that consist of 20 nm TiO$_2$ nanocrystallites sensitized by ruthenium-based dyes.[1] ZnO is a versatile, wide-bandgap semiconductor and has recently been reported as an alternative for DSCs because ZnO offers a large direct band gap of 3.37 eV, which is similar to TiO$_2$ and has very high electron mobility, which is about 155 cm^2 V^{-1} s^{-1} for high-quality thin film.[6] ZnO also can be tailored to various nanostructures as compared to TiO$_2$, which provides a promising means for improving the performance of the photoelectrode in DSCs.[7]

Competition between the generation and recombination of photoexcited carriers in DSCs is a main bottleneck for developing higher conversion efficiency. 1D nanostructures, such as nanowires[8–10] and nanotubes[11–13] have been extensively used, as the aim is expected to significantly improve the electron transport efficiency in the photoelectrode films by providing a direct conduction pathway for the rapid collection of photogenerated electrons and, therefore, reduce the number of interparticle hops. Furthermore, the immersion of a sensitizer into an array of nanowires with vertical pores should prove easier than the more tortuous pores of a nanoparticle film. However, insufficient internal surface area of those 1D nanostructures limits the energy conversion efficiency at a relatively low level, for example, 1.5% for ZnO nanowires[8] and 4.7% for TiO$_2$ nanotubes.[12] Another approach to overcome the problem was the incorporation of nanoparticles

with original 1D nanostructures.[14,15] The nanowires/nanoparticles composite was mainly ascribed to enrich the light harvesting without sacrificing the electron-transport efficiency. Even so, the excess electron hoping through the interparticle barriers might still reveal the chance of charge recombination. In this regard, the nanostructures of tiny hierarchical nanobuilding units into larger organized conformations and geometrical architectures are intensely desirable from both the structural design and proposed application points of view. On the basis of the chemical vapor deposition (CVD), Suh et al.[16] and Baxter and Aydil[17] have presented the dendritic ZnO nanowires and their efficiencies of about 0.5%. The relative low-energy conversion for the early reports was due to insufficient surface area of the branched ZnO nanowires. On the other hand, Kar and Santra[18] recently fabricated the paint-brush-like ZnO nanostructures from the solvothermal approach and predicted the self-assembled hierarchical nanostructures could be appropriate not only in multiport contact probes but also are suitable for dye-sensitized solar cell applications because of their large surface areas. Moreover, Jiang et al.[19] reported the ZnO-nanoflower photoanode via a hydrothermal method and had the 1.9% efficiency in DSCs for which was the highest efficiency in ZnO nanowire-based DSCs to date. Accordingly, aqueous solution method is one of the remarkable approaches to fabricate functional and dense hierarchical ZnO nanostructures such as the photoelectrode in DSCs from the low cost and mass production requirements.

In the present work, we fabricated the treelike branched ZnO nanowire structures via a simple solvothermal method. The 1D secondary branches directly attached to the main ZnO nanowire backbone could simultaneously afford a direct conduction pathway and achieve the higher dye adsorption to significantly enhance the overall efficiency of the DSCs.

II. Experimental Section

Synthesis of Branched ZnO Nanowire Arrays. The branched ZnO nanowires were fabricated from a modified aqueous solution method similar to Law et al.[8] First, the arrays of ZnO nanowires were synthesized on seeded fluorine-doped tin oxide (FTO) substrates (10 Ω per square, Nippon Sheet Glass) by

* To whom the correspondence should be addressed: Tel: +886-3-5712121, ext. 56316. Fax: +886-3-5716631. E-mail: wfhsieh@mail.nctu.edu.tw.
† National Chiao Tung University.
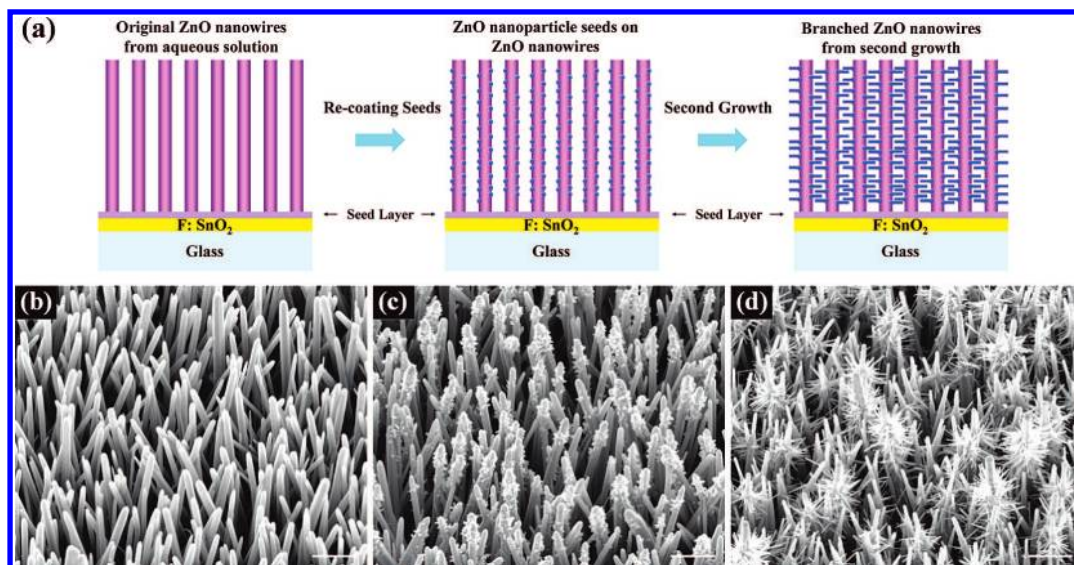‡ Industrial Technology Research Institute.

Figure 1. (a) The schematic growth procedure from the original ZnO nanowires to the branched ZnO nanowires, (b) before and (c) after recoating a seed layer of the original ZnO nanowires obtained from a solvothermal method, and (d) the branched ZnO nanowires after second growth; scale bar, 1 μm.

immersing the seeded substrates in aqueous solutions containing 0.08 M zinc nitrate hydrate (98%, Riedel-deHaën), 0.08 M hexamethylenetetramine (99%, Showa), and 12 mM polyethylenimine (branched, low molecular weight, Aldrich) at 95 °C for 10 h. Second, the ZnO nanowires substrate obtained from the first step were recoated with seed layers of ZnO nanoparticles by dip-coating in a 0.005 M zinc acetate dihydrate ($Zn(OAc)_2$) (99%, Riedel-deHaën) in ethanol. Then the branched nanowires were grown by immersing the seeded ZnO nanowires in aqueous solutions containing 0.02 M zinc nitrate hydrate, 0.02 M hexamethylenetetramine, and 3 mM polyethylenimine at 95 °C for 5 h. The branched ZnO nanowires were finally rinsed with deionized water and baked in air at 450 °C for 30 min to remove any residual organics.

Cell Fabrication and Characterization. Solar cells were prepared by immersing the branched ZnO nanowires on conductive glass substrates into a solution of 0.5 mM cis-bis(isothiocyanato)bis(2,2′-bipyridyl-4,4′-dicarboxylato)-ruthenium(II) bis-tetrabutylammonium (N719, Solaronix) in acetonitrile/*tert*-butanol (1:1) for 20 min, and the films were then rinsed with acetonitrile. The sensitized electrodes were sandwiched together with thermally platinized FTO counter electrodes separated by 25 μm thick hot-melt spacers (Surlyn, Dupont). The internal space of the cell was filled with an electrolyte solution (0.1 M LiI, 0.5 M 1,2-dimethyl-3-propylimidazolium iodide, 0.03 M I_2, and 0.5 M *tert*-butylpyridine in acetonitrile). The area of active electrode was typically 0.28 cm^2. Efficiencies for solar energy conversion and ac impedance spectroscopy were immediately evaluated under AM 1.5 simulated sunlight (Yamashita Denso, YSS-100A) with an electrochemical analyzer (Autolab, PGSTAT3). The light power was calibrated with a set of neutral density filters using a silicon photodiode (BS-520, Bunko Keiki).

Instrumentation. The morphologies and dimensions were characterized using a JEOL-6500 field emission scanning electron microscope (FESEM) operated at 5 KeV. The advanced microstructures of ZnO nanostructures were analyzed using JEOL JEM-2100F field emission transmission electron microscope (FETEM) operated at 200 KeV. The phases were characterized using a Bede D1 thin film X-ray diffractometer (TFXRD). Raman spectroscopy was carried out using a frequency-doubled Yb:YAG laser ($\lambda = 515$ nm) on a Jobin-Yvon

T64000 microspectrometer with a 1800 grooves/mm grating in a backscattering configuration. Dye loading was determined by detaching the dye from the ZnO photoelectrode surface with 0.1 M NaOH solution and measuring the optical absorbance with a Hitachi U-2800 UV−vis spectrophotometer.

III. Results and Discussion

The formation mechanism of the branched ZnO nanowires is illustrated in part a of Figure 1 and its corresponding FESEM images in parts b−d of Figure 1. Part b of Figure 1 shows the bare ZnO nanowires with a slight vertical off-alignment were grown perpendicularly on the FTO substrate using a solvothermal method. Through the precoating process on the ZnO nanowires, little crystalline nanopaticles with a diameter of 10−20 nm were formed on the backbone nanowires, as shown in part c of Figure 1. After the second growth step, radial secondary ZnO branches emanated from the seeds, as shown in part d of Figure 1. Figure 2 presents the large-scale and magnified FESEM micrographs of branched ZnO arrays. The branched ZnO nanostructures were fabricated over the entire substrate with a density of backbone nanowire about 7×10^8 cm^{-2}. The backbone nanowires have length and diameter in the range of 7−8 μm and 150−250 nm, respectively, whereas the secondary branches have length and diameter ranging from 100−300 nm and 20−50 nm, respectively. The branched ZnO nanowires can be fabricated by the infiltration of moderate concentrated $Zn(OAc)_2$ solution into interstitial voids between backbone ZnO nanowires. However, the secondary branches were not produced on the surface of each ZnO backbone. The lack of uniformity of secondary branches can be interpreted as the results of rough dip-coating processes that cause nonuniform infiltration and finally lead to randomly disturbed seed layers upon the backbone ZnO nanowires. Moreover, in some conditions, the seed layers hardly infiltrate into the deep side-wall of original ZnO nanowires during the immersion but left as coverage upon the ZnO nanowires (Supporting Information, Figure S1). Those failed conditions would mostly occur when using more concentrated $Zn(OAc)_2$ solution and also when the substrates were heated during dip-coating. The fast crystallization would lead the aggregation of ZnO seed layers and consequently blocked the infiltration of subsequent aqueous solutions.
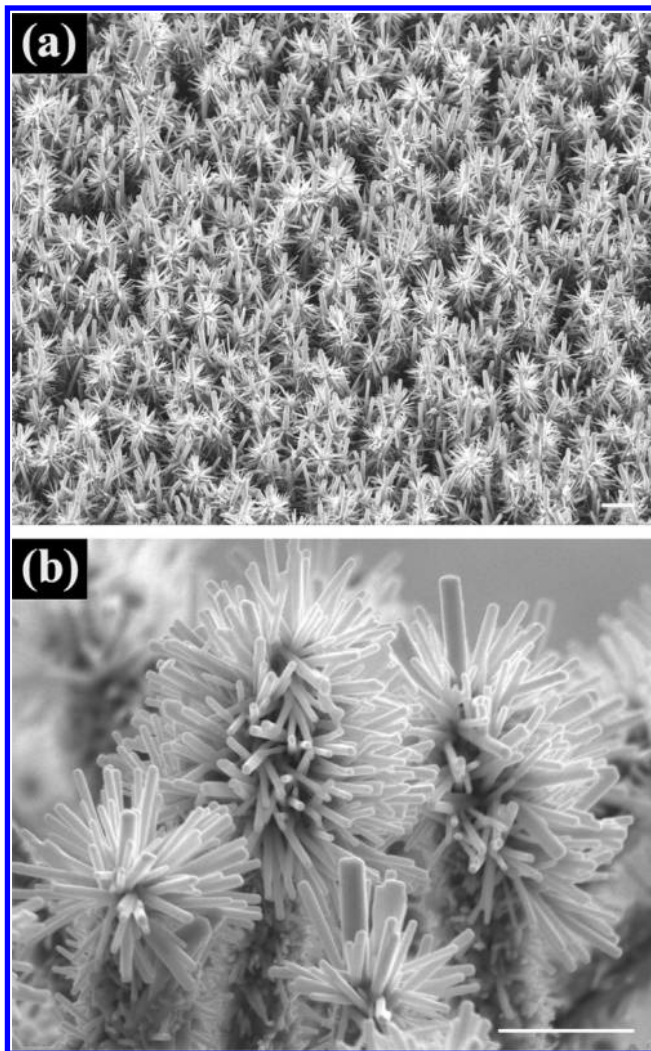
Formation of Branched ZnO Nanowires

J. Phys. Chem. C, Vol. 112, No. 42, 2008 **16361**

Figure 2. (a) Low- and (b) high-magnification FESEM images of the branched ZnO nanowires after second growth; scale bar, 1 μm.

Further structural characterizations of the branched ZnO nanowires were performed with TEM. Unlike the other reports of comblike ZnO nanostructures, which demonstrated the monolithically single-crystalline relationship between the branches and backbone nanowires,[20,21] in the present mechanism, the secondary ZnO branches were fabricated merely on the ZnO seeds regardless of the coordinate crystal relationship. Part a of Figure 3 displays the secondary ZnO branches, which were grown on the side walls of nanowire backbones with different radial angles. The evidence confirmed the secondary ZnO branches were not the derivatives of ZnO nanowires but definitely originated from the small crystallite ZnO seeds via our precoating process. The magnified intersection area of ZnO branch and nanowire was shown in part b of Figure 3. Parts c and d of Figure 3 show the corresponding nanobeam diffraction (NBD) of the secondary ZnO branch and select-area electron diffraction (SAED) of the ZnO nanowire backbone, respectively. The diffraction patterns confirmed the each ZnO nanostructure was preferentially oriented in the c axis direction with the single-crystal wurtzite structure even though the two components of ZnO nanostructures were not fabricated simultaneously.

Part a of Figure 4 shows the $\theta-2\theta$ X-ray diffraction patterns of ZnO nanostructures, which corresponds to the presence of hexagonal wurtzite crystallites with cell constants of $a = 3.251$ Å and $c = 5.208$ Å. The strong {0001} diffraction family of ZnO indicates that the nanowires are moderately oriented in

the c axis direction. No excess peaks were detected, which indicates that all of the precursors have been completely decomposed. Because the wurtzite structure of ZnO belongs to the space group $C_{6v}^4(P6_3mc)$, one primitive cell includes two formula units, with all of the atoms occupying $2b$ sites of symmetry C_{3v}. Group theory predicts the existence of the following optic modes: $A_1 + 2B_1 + E_1 + 2E_2$ at the Γ point of the Brillouin zone; B_1 (low) and B_1 (high) modes are normally silent; A_1, E_1, and E_2 modes are Raman active; and A_1 and E_1 also are infrared active. Thus, A_1 and E_1 are split into longitudinal (LO) and transverse (TO) optical components. Part b of Figure 4 shows a Raman spectrum of the branched ZnO nanowires, which was taken with an accumulation time of 120 s from a 5 μm spot size excited by a frequency-doubled Yb:YAG laser ($\lambda = 515$ nm). As we can see, the remarkable E_2 (low) and E_2 (high) mode of ZnO are located at 98 and 438 cm^{-1}, respectively. The peak at 332 cm^{-1} can be assigned to the second-order Raman scattering arising from zone-boundary phonons 2-E_2(M) of ZnO. The weak and almost invisible signal around 581 cm^{-1} is contributed to the superimposition of A_1(LO) and E_1(LO). No substrate signals appeared because of the penetration limitation of 515 nm laser light. The good crystalline quality of ZnO nanostructures confirmed above ensure that the photoelectrode can offer good electronic conductivity and avoid the electron trapping within the structural defects.

Part a of Figure 5 shows the compared photocurrent−voltage (J−V) characteristics for solar cells, constructed using the bare ZnO nanowires and the branched ZnO nanowires, with AM 1.5 illumination at 100 mW/cm^2 from a xenon lamp. The short-circuit current density (J_{sc}) and the overall light conversion efficiency of the branched ZnO nanowire DSCs were 4.27 mA/cm^2 and 1.51%, respectively, which are almost twice higher than that of the bare ZnO nanowires. Table 1 summarizes the measured and calculated values obtained from each J−V curve. One factor for the increment in short-circuit current density would be the enhanced photon absorption associated with the presence of enlargement of internal surface area resulting in sufficient dye-loading. Although the length and density of ZnO structures exhibit the disadvantage compared with previous studies,[8] the overall efficiency can achieve almost the same value via utilizing the extra secondary nanobranches. The values of fill factor (FF) for ZnO DSCs are general lower than those using TiO$_2$ nanoparticles (0.6−0.7). This is attributed to recombination between photoexcited carriers in the photoanodes and tri-iodide ions in the electrolyte. A slightly different value in the bare ZnO nanowire and branched ZnO nanowire DSCs revealed almost the same interfacial recombination, which was evidenced by the equivalent value of the shunt resistance $R_{sh} = (dV/dI)_{V=0}$ from the I−V curves under illumination. The series resistance $R_s=(dV/dI)_{I=0}$ for branched ZnO nanowire DSCs (25.64 Ωcm^2) was significantly lower than the bare ZnO nanowire ones (46.13 Ωcm^2) and was previously explained association with the dye loading but not the nanowire length.[10]

Recently, electrochemical impedance spectroscopy (EIS) measurement has been widely performed to investigate electronic and ionic processes in DSCs.[22−28] The Nyquist plots of the impedance data for bare and branched ZnO nanowire DSCs were performed by applying a 10 mV ac signal over the frequency range of 10^{-2} to 10^5 Hz under illumination at the applied bias of V_{oc}, as shown in part b of Figure 5. Some interior parameters of the devices with a thickness of L_F can be derived by well fitting the impedance data of the Nyquist plots to expressions based on the modified equivalent circuit of nanowire DSCs suggested by Wu et al.[26,27] In fact, the concrete equivalent
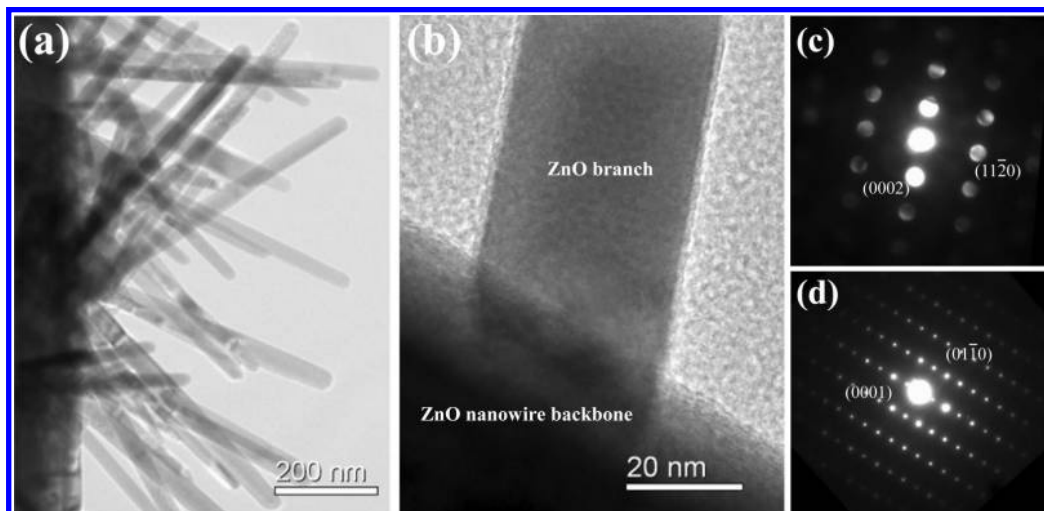
Figure 3. (a) TEM image of a single branched ZnO nanowire, (b) the magnified intersection area of ZnO branch and nanowire, and (c and d) the corresponding nanobeam diffraction (NBD) and select-area electron diffraction (SAED) for the secondary ZnO branch and the ZnO nanowire backbone, respectively.
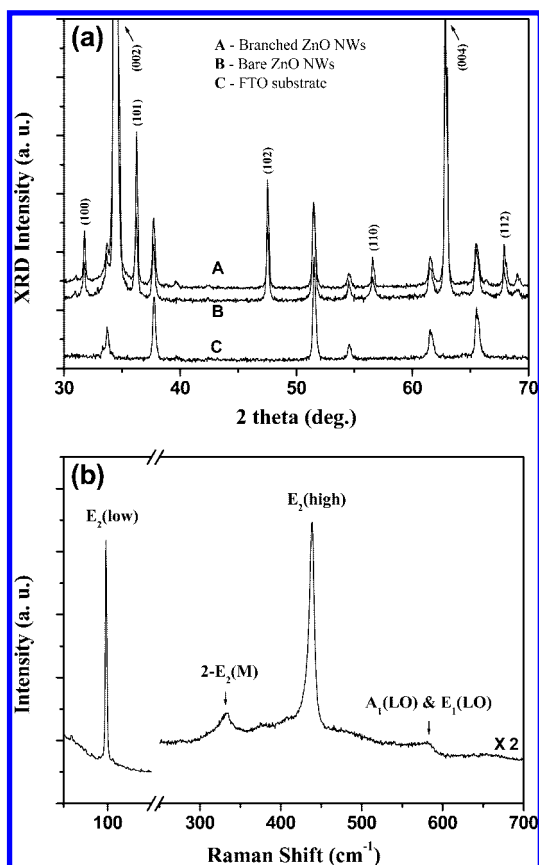

Figure 4. (a) $\theta-2\theta$ XRD profiles of A, the branched ZnO nanowires; B, the bare ZnO nanowires on the fluorine doped tin oxide substrate; and C, fluorine-doped tin oxide substrate only. (b) Raman spectra of the branched ZnO nanowires, using a frequency-doubled Yb:YAG laser ($\lambda = 515$ nm).

Figure 5. (a) Current density against voltage (J-V) characteristics and (b) Nyquist plots of the bare ZnO nanowires and the branched ZnO nanowire DSCs. The solid lines in (b) are the fitting results based on the equivalent circuit model (modified from ref 23) as shown in the inset. r_w is the transport resistance of the electrons in the ZnO electrode; r_k is the charge-transfer resistance of the charge recombination between electrons in the ZnO electrode and I_3^- in the electrolyte; The thickness L_F of all anodes are about 8 μm; $C_\mu = (c_\mu L_F)$ is the chemical capacitance of the ZnO electrode; R_s is a series resistance for the transport resistance of FTO and all resistances out of the cell; Z_N is the impedance of diffusion of I_3^- in the electrolyte; R_{Pt} and C_{Pt} are the charge-transfer resistance and the interfacial capacitance at the counter electrode (platinized FTO glass) /electrolyte interface, respectively; R_{FTO} and C_{FTO} are the charge-transfer resistance and the interfacial capacitance at the exposed FTO/electrolyte interface, respectively; R_{FZ} and C_{FZ} are the resistance and the capacitance at the FTO/ZnO contact, respectively.

circuit might be more complex in the operation of the DSC devices. Mora-Seró et al. have recently reported a negative capacitance for different types of solar cells, that is, an inductive behavior that comes from the conductivity modulation of the electrolyte by injected electrons from the photoelectrode when providing high forward bias with low frequency.[24] Hence, the impedance data obtained at different applied potentials cannot be fitted with a single equivalent circuit. An essential component such as an inductive response was suggested to be considered
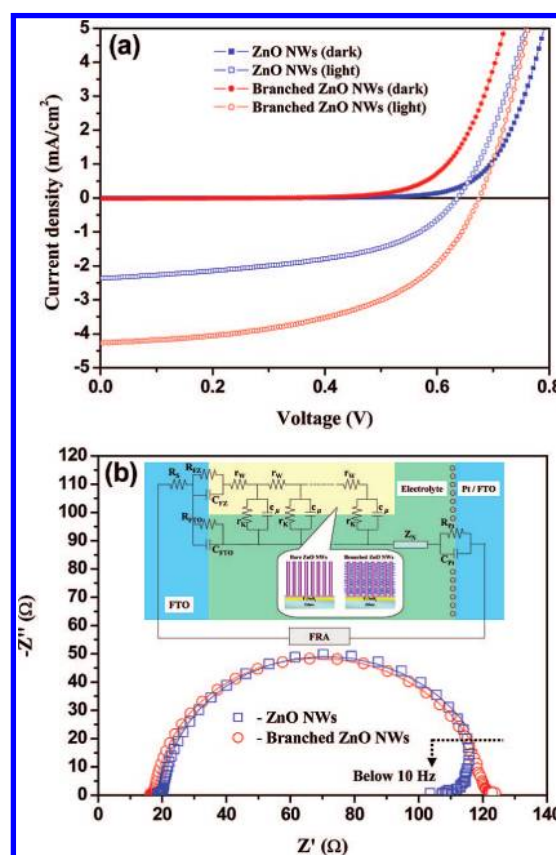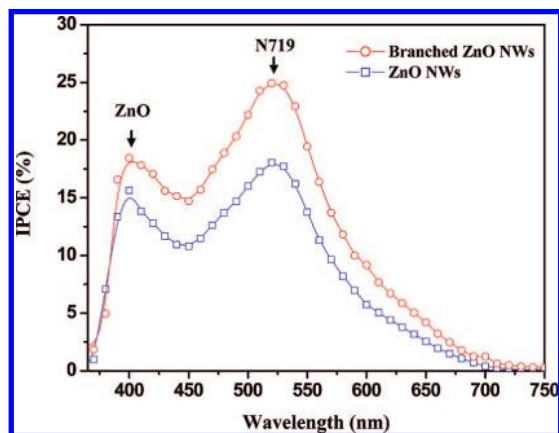
TABLE 1: Performances and Electron Transport Properties of the Bare ZnO Nanowire and the Branched ZnO Nanowire DSCs Determined by Photocurrent Density−Voltage (J-V) Characteristics and Electrochemical Impedance Spectroscopy (EIS) Analysis

ZnO DSCs	J_{sc} (mA/cm^2)	V_{oc} (V)	FF	η (%)	k_{eff} (s^{-1})	τ_{eff} (s)	R_k (Ω)	R_w (Ω)	D_{eff} (cm^2/s)
bare nanowires	2.37	0.636	0.498	0.75	38.31	0.026	92.12	3.63	6.23×10^{-4}
branched nanowires	4.27	0.675	0.522	1.51	26.31	0.038	86.85	3.36	4.35×10^{-4}

in series with a recombination resistance. To avoid the unnecessary interference from the inductive behavior, we presently ignored the low-frequency part of impedance data. The fitted results were also listed in Table 1, which include the first-order reaction rate constant for the loss of electrons (k_{eff}), the electron lifetime ($\tau = 1/k_{eff}$), the electron transport resistance ($R_w = r_w L_F$) and the charge transfer resistance related to recombination of electron at the ZnO/electrolyte interface ($R_k = r_k/L_F$). We found R_k and R_w are quite similar for both DSCs in this present work, which indicated the same interfacial recombination and equal crystallinity for either bare ZnO nanowires or branched ZnO nanostructures. On the contrary, k_{eff} in the branched ZnO nanowire DSCs was smaller than the bare nanowire ones to cause the smaller effective diffusion length[25] ($D_{eff} = (R_k/R_w)L_F^2 k_{eff}$) in branched ZnO nanowire DSCs. Because k_{eff} is related to reaction rate, the electron lifetime ($\tau_{eff} = 1/k_{eff}$) could be prolonged by the additional transport distance between branches and conductive electrode.

In general, the current density for DSCs is determined by the initial number of photogenerated carriers, the electron injection efficiency from dye molecules to semiconductor, and the recombination rate between the injected electrons and oxidized dye or redox species in the electrolyte. On the basis of the assumption of the same injection efficiency and recombination rate for the given ZnO DSCs systems, it is reasonable that the initial number of photogenerated carriers may be significantly affected by the variation in the light-harvesting capability of differently structured photoanodes. Figure 6 displays the wavelength distribution of incident monochromatic photon to current conversion efficiency (IPCE). The photocurrent peaks occurring at approximately 400 nm were due to direct light harvesting by ZnO semiconductor, in which the photogenerated electrons diffused through ZnO and the holes in the valence band were replenished directly by charge transfer from the I_3^-/I^- electrolyte.[10] The maxima of IPCE at approximately 525 nm are contributed by the dye absorption, corresponding to the visible $t_2 \rightarrow \pi^*$ metal-to-ligand charge transfer (MLCT). The IPCE obtained for the branched ZnO nanowire DSCs was

almost 1.5 times that of the bare ZnO nanowire. The improvement in the IPCE suggested that the high-energy conversion efficiency results predominantly from sufficient dye-loading by branched ZnO nanowires, which enlarged internal surface area within the photoelectrode. The dye loading of the photoelectrodes was measured to determine the surface concentration of dye molecules adsorbed on different ZnO nanostructures (Supporting Information, Figure S2). The concentration of dye in the branched ZnO nanowire electrode was found to be 2.9×10^{-9} mol/cm^{-2} as measured from dye-desorption experiments, which is almost 40% higher than the obtained value of 2.1×10^{-9} mol/cm^{-2} for the bare ZnO nanowire electrode. It is important to note that the dye loading of the branched ZnO nanowires was not twice as high as the value of the bare ZnO nanowires, even though the current density and energy conversion efficiency of the branched ZnO nanowire DSCs are twice as high as the bare ZnO nanowire ones. The different could be ascribed to the insufficient internal surface of the bare ZnO nanowires and the excess dye, which resulted in the formation of Zn^{2+}/dye complexes instead of the effective chemical bonding between ZnO and dye molecular.[29] The shorter immersion time for deficient chemical-stability ZnO electrode as compared with TiO$_2$ electrode have recently been reported in detail by Chou et al.[30] Therefore, the excess immersion time for the insufficient internal surface of bare ZnO nanowires could not achieve more dye loading but seriously deteriorate the performance of DSCs.

The concept of the branched nanostructures is anticipated to be applicable to other semiconductor photoelectrodes in organic−inorganic nanocomposite solar cells and branched heterojunction nanostructures for future applications. Although the secondary branches had nonuniform distribution, the branches emanated from partial ZnO nanowires because of the simple dip-coating process, and they still can offer greater effective surface area for dye adsorption than the bare nanowires. For optimization of the filling factor of the ZnO nanostructures, the dc or radio frequency magnetron sputtering and atomic layer deposition might be a great benefit to the precoating processes. Further improvement of energy conversion efficiency could be implemented through adjusting denser and longer branches to fill the interstitial voids between backbone nanowires, which will substantially improve light harvesting and the current density.

IV. Conclusion

In summary, branched ZnO nanowires have been fabricated on FTO substrates using a solvothermal method for DSCs. The short-circuit current density and the overall light-conversion efficiency of the branched ZnO nanowire DSCs were almost twice as high as the bare ZnO nanowire ones. The improvement can be explained in association with the enlargement of the internal surface area within the photoelectrode without increasing interparticle hops. In addition, the sufficient dye-loading in branched ZnO nanowire DSCs was further evidenced from the lower series resistance $R_s = (dV/dI)_{I=0}$ and dye-desorption measurement. The branched ZnO nanowires significantly enhanced IPCE spectra as compared with the bare ZnO nanowires.

Figure 6. Incident monochromatic photon to current conversion efficiency (IPCE) of the bare ZnO nanowire and the branched ZnO nanowire DSCs.

Therefore, the concept of these 1D branched nanostructures could simultaneously afford a direct conduction pathway and achieve higher dye adsorption to significantly enhance the overall energy conversion efficiency of the DSCs.

Supporting Information Available: Cross section FESEM images of branched ZnO nanowires. Optical absorption of dye unloaded from the bare ZnO nanowire and the branched ZnO nanowire substrates. This material is available free of charge via the Internet at http://pubs.acs.org.

References and Notes

(1) Grätzel, M. *Inorg. Chem.* **2005**, *44*, 6841.

(2) Nazeeruddin, M. K.; DeAngelis, F.; Fantacci, S.; Selloni, A.; Viscardi, G.; Liska, P.; Ito, S.; Takeru, B.; Grätzel, M. *J. Am. Chem. Soc.* **2005**, *127*, 16835.

(3) Keis, K.; Magnusson, E.; Lindstrom, H.; Lindquist, S. E.; Hagfeldt, A. *Sol. Energy Mater. Sol. Cells* **2002**, *73*, 51.

(4) Stergiopoulos, T.; Arabatzis, I. M.; Cachet, H.; Falaras, P. *J. Photochem. Photobiol. A* **2003**, *155*, 163.

(5) Guo, P.; Aegerter, M. A. *Thin Solid Films* **1999**, *351*, 290.

(6) Kaidashev, E. M.; Lorenz, M.; von Wenckstern, H.; Rahm, A.; Semmelhack, H. C.; Han, K. H.; Benndorf, G.; Bundesmann, C.; Hochmuth, H.; Grundmann, M. *Appl. Phys. Lett.* **2003**, *82*, 3901.

(7) Wang, Z. L. *Materials Today* **2004**, *7*, 26.

(8) Law, M.; Greene, L. E.; Johnson, J. C.; Saykally, R.; Yang, P. *Nat. Mater.* **2005**, *4*, 455.

(9) Baxter, J. B.; Aydil, E. S. *Appl. Phys. Lett.* **2005**, *86*, 053114.

(10) Pasquier, A. D.; Chen, H.; Lu, Y. *Appl. Phys. Lett.* **2006**, *89*, 253513.

(11) Wang, H.; Yip, C. T.; Cheung, K. Y.; Djurišić, A. B.; Xie, M. H.; Leung, Y. H.; Chan, W. K. *Appl. Phys. Lett.* **2006**, *89*, 023508.

(12) Mor, G. K.; Varghese, O. K.; Paulose, M.; Shankar, K.; Grimes, C. A. *Sol. Energy Mater. Sol. Cells* **2006**, *90*, 2011.

(13) Zhu, K.; Neale, N. R.; Miedaner, A.; Frank, A. J. *Nano Lett.* **2007**, *7*, 69.

(14) Tan, B.; Wu, Y. *J. Phys. Chem. B* **2006**, *110*, 15932.

(15) Ku, C. H.; Wu, J. J. *Appl. Phys. Lett.* **2007**, *91*, 093117.

(16) Suh, D. I.; Lee, S. Y.; Kim, T. H.; Chun, J. M.; Suh, E. K.; Yang, O. B.; Lee, S. K. *Chem. Phys. Lett.* **2007**, *442*, 348.

(17) Baxter, J. B.; Aydil, E. S. *Sol. Energy Mater. Sol. Cells* **2006**, *90*, 607.

(18) Kar, S.; Santra, S. *J. Phys. Chem. C* **2008**, *112*, 8144.

(19) Jiang, C. Y.; Sun, X. W.; Lo, G. Q.; Kwong, D. L.; Wang, J. X. *Appl. Phys. Lett.* **2007**, *90*, 263501.

(20) Yan, H.; He, R.; Johnson, J.; Law, M.; Saykally, R.; Yang, P. *J. Am. Chem. Soc.* **2003**, *125*, 4728.

(21) Wang, Z. L.; Kong, X. Y.; Zuo, J. M. *Phys. Rev. Lett.* **2003**, *91*, 185502–1.

(22) Wang, Q.; Moser, J. E.; Grätzel, M. *J. Phys. Chem. B* **2005**, *109*, 14945.

(23) Wang, Q.; Ito, S.; Grätzel, M.; Fabregat-Santiago, F.; Mora-Seró, I.; Bisquert, J.; Bessho, T.; Imai, H. *J. Phys. Chem. B* **2006**, *110*, 25210.

(24) Mora-Seró, I.; Bisquert, J.; Fabregat-Santiago, F.; Garcia-Belmonte, G.; Zoppi, G.; Durose, K.; Proskuryakov, Y.; Oja, I.; Belaidi, A.; Dittrich, T.; Tena-Zaera, R.; Katty, A.; Lévy-Clément, C.; Barrioz, V.; Irvine, S. J. C. *Nano Lett.* **2006**, *6*, 640.

(25) Adachi, M.; Sakamoto, M.; Jiu, J.; Ogata, Y.; Isoda, S. *J. Phys. Chem. B* **2006**, *110*, 13872.

(26) Wu, J. J.; Wang, D. K. P. *Adv. Mater.* **2007**, *19*, 2015.

(27) Wu, J. J.; Chen, G. R.; Yang, H. H.; Ku, C. H.; Lai, J. Y. *Appl. Phys. Lett.* **2007**, *90*, 213109.

(28) Lin, C. J.; Yu, W. Y.; Chien, S. H. *Appl. Phys. Lett.* **2007**, *91*, 233120.

(29) Horiuchi, H.; Katoh, R.; Hara, K.; Yanagida, M.; Murata, S.; Arakawa, H.; Tachiya, M. *J. Phys. Chem. B* **2003**, *107*, 2570.

(30) Chou, T. P.; Zhang, Q.; Cao, G. *J. Phys. Chem. C* **2007**, *111*, 18804.

JP805239K